E3S Web of Conferences **573**, 01009 (2024) https://doi.org/10.1051/e3sconf/202457301009
SDER 2024

Influence of carbide tooth grinding parameters on shaping efficiency of high steel grade tubing

Geng Tang[1*], Qiang Liu[2], Xue Li[1], Liangliang Ding[3], Lin Zhang[1], Xing Yang[2], Hao Gong[1]

[1]Engineering Technology Research Institute,Petro China Southwest Oil&Gasfield Company, Chengdu, Sichuan Province, 610056, China
[2]Engineering Technology Department of PetroChina Southwest Oil and Gasfield Company, Chengdu, Sichuan Province, 610056, China
[3]Southwest Petroleum University School of Mechatronic Engineering, Chengdu, Sichuan Province, 610500, China

Abstract: Complex oil and gas well service conditions very easily trigger downhole casing deformation and failure, resulting in most of the oil and gas field casing shaping and repairing the difficulty of rising, casing micro-plasticity and micro-expansion technology can effectively solve the problem of casing local shrinkage and bending and deformation, in order to study the grinding shoe alloy teeth cloth angle, grinding speed and grinding depth on the grinding force change rule, according to the grinding theory to establish a single tooth and casing microelement section plane numerical model Model, the use of Johnson-Cook damage isomorphism model to characterize the material dynamic cutting failure, through the numerical simulation results fitted to the grinding force as the dependent variable, alloy tooth angle, speed, depth of grinding for the independent variables of the evaluation formula. The analysis results show that the grinding force decreases with the change of alloy tooth front angle from 0° to 60°; the grinding force does not change significantly in the range of milling speed from 40r/min to 80r/min; and the grinding force increases gradually when the milling depth increases. It is concluded that the angle and depth of the alloy tooth front are the main controlling factors for controlling the grinding and milling capacity, and this understanding provides technical references for the design and optimization of casing repair and is of great significance for accurately predicting the shaping capacity of the deformed casing and ensuring the integrity of the wellbore.

1. Introductory

With the increasing global thirst for energy, the exploration and production of oil and natural gas have become increasingly important [1]. China's relatively small oil and gas reserves, coupled with the complex geological conditions in which the oil and gas resources are located, have led to high domestic oil and gas production costs and insufficient international competitiveness [2]. With the gradual depletion of conventional oil and gas resources, China's oil and gas exploration and production is gradually shifting to deep wells, ultra-deep wells, and operations under complex conditions such as tight oil and gas. For example, the average drilling depth of the Sichuan oil and gas field in the northwest of Sichuan has reached 6,689 meters, with the deepest reaching 7,793 meters. The Xinjiang Tarim oilfield drilled China's first 10,000-metre deep well, the Deep Earth Tarko 1 well, on 30 May 2023 [3]. Exploration and production of ultra-deep wells have helped to reveal the distribution and reserves of deep inland oil and gas resources in China, providing key data for the development of deep oil and gas resources. However, affected by geological structures, engineering challenges , and corrosion, ultra-deep oil and gas wells often suffer from casing deformation, especially in formations prone to collapse and those with severe plastic creep and poor cementing quality. This situation can have a serious impact on the safety and efficiency of oil and gas fields, so casing repair technology becomes particularly critical in the mid-and late-stage exploitation of oil fields [4].

Scholars at home and abroad have carried out a large number of studies on the problem of deformed casing repair. Shen Huanyu [5] conducted a strength analysis study on the carbide tooth structure of small-size tooth wheel drills, established three kinds of tooth models, conducted static strength analysis of carbide teeth through numerical simulation methods, obtained the tooth structure Mises stress distribution, and structural optimization of the wedge-shaped teeth with poor strength; Fan Jaxing [6], in response to the problem of casing damage, developed a new type of mechanical-hydraulic composite casing Finally, the feasibility of mechanical-hydraulic composite casing shaping technology is confirmed through the comparison of pear-shaped expander technology and composite casing shaping technology on-site application; Wu Zebing [7], for the low drilling efficiency of drillable composite bridge plug technology in horizontal wells and the difficulty of returning chips and other problems, took the dorsal plate of the thoracic node of dung beetles of the soil animal as the bionic prototype, and designed a kind of bionic pregnant with diamond centring shoes, which is found

* Corresponding author: tanggeng2024@163.com

that the bionic grinding shoe drills and grinds the casing through the comparison with the conventional grinding shoes. It is found that the bionic grinding shoe has a faster drilling and grinding speed, a higher success rate of chip return, and a lower possibility of jamming the drill; Kuanhai Deng [8] established a mechanical model of the rotary shaper and the deformed casing based on the Hertzian contact theory, analyzed the axial load and circumferential deformation of the deformed casing by using dynamics to determine the working load of the rotary shaper, and finally carried out the repair test of the deformed casing, which verified the accuracy of the mechanical model. accuracy of its mechanical model. The above scholars have provided research ideas for the problem of repairing deformed casing, but the current research on repairing deformed casing for grinding shoes is still insufficient, based on which, this paper carries out a simulation study on the micro-segment of grinding casing with a single carbide tooth on a grinding shoe.

In order to clarify the working condition of alloy teeth in the process of grinding shoe repairing deformed casing, this paper adopts a numerical simulation method to establish the two-dimensional plane model of single alloy teeth and casing microelement segment. The mechanical state of the alloy teeth and casing during the grinding process is characterized by the Johnson-Cook dynamic principal model, and the JC principal and damage model of the casing material is obtained based on the uniaxial tensile experiment of the casing material. Finally, by changing the alloy tooth grinding front angle, milling speed , and milling depth, the influence laws of the three variables on the alloy tooth grinding force during the milling process were investigated and empirical equations were fitted. It is concluded that the alloy tooth grinding front angle and depth are the main controlling factors for controlling the grinding and milling capacity, and this understanding provides technical references for casing repair design and optimization, as well as important significance for accurately predicting the plastic capacity of deformed casing and ensuring wellbore integrity.

2. Simulation study of alloy tooth grinding and milling casing

2.1. P110 casing material constitutive model

The Johnson-Cook intrinsic model has the advantages of a concise equation form and easy-to-fit material coefficients, and it also takes into account the effects of strain hardening, strain rate strengthening, and temperature softening effects, which can accurately reflect the mechanical properties of the material under the conditions of large strains, high strain rates, and high temperatures [9-11]. This model has been widely used in the field of milling and milling finite element numerical simulation, and its expression is:

$$\sigma = (\mathrm{A}+\mathrm{B}\varepsilon_p^n)(1+\mathrm{C}\ln\frac{\dot{\varepsilon}}{\dot{\varepsilon}_0})(1-\mathrm{T}^{*\mathrm{m}}) \quad (1)$$

In Eq. (1) σ is the flow stress (Pa); A, B, C, n, and m are five parameters to be determined. Where A is the initial yield stress; B is the hardening constant; n is the dimensionless hardening coefficient; C is the strain rate sensitivity; m is the thermal sensitivity; $\dot{\varepsilon}_0$ is the reference strain rate (1/s); $\dot{\varepsilon}$ is the loading strain rate (1/s); and the expression of $T^{*\mathrm{m}}$ can be expressed as:

$$T^{*\mathrm{m}} = \left(\frac{T-T_\mathrm{r}}{T_\mathrm{m}-T_\mathrm{r}}\right)^\mathrm{m} \quad (2)$$

Eq. (2) where T is the current temperature; Tr is the room temperature; and Tm is the melting temperature.

1)Fitting parameters A, B, n

When at room temperature conditions (i.e., $T=T_\mathrm{r}$), such that $\dot{\varepsilon}=\dot{\varepsilon}_0$, then the expression for the JC eigenmodes can be simplified as:

$$\sigma = (\mathrm{A}+\mathrm{B}\varepsilon_p^n) \quad (3)$$

The yield stress of the material when $\varepsilon=0$ is the value of A, obtained by taking logarithms at the ends of equation (3):

$$\ln(\sigma\text{-A})=\ln\mathrm{B}+n\ln\varepsilon \quad (4)$$

Make an $\ln(\sigma\text{-A})\text{-}\ln\varepsilon$ curve, the intercept of the curve is lnB and the slope is n.

2)The fitting parameters C

When at room temperature conditions (i.e., $T=T_\mathrm{r}$), so that $\varepsilon=0$, i.e., when the plastic strain of the material is zero, the expression for the JC principal structure can be simplified to:

$$\sigma = (1+\mathrm{C}\ln\frac{\dot{\varepsilon}}{\dot{\varepsilon}_0}) \quad (5)$$

The value of C was fitted by making a $\sigma\text{-}\ln\frac{\dot{\varepsilon}}{\dot{\varepsilon}_0}$ curve from the $\sigma\text{-}\varepsilon$ relation obtained at room temperature.

3)The fitting parameters m

Let $\varepsilon=0$ and $\dot{\varepsilon}=\dot{\varepsilon}_0$. The expression for the JC principal structure can be simplified as:

$$\sigma=A(1-\left(\frac{T-T_\mathrm{r}}{T_\mathrm{m}\text{-}T_\mathrm{r}}\right)^\mathrm{m}) \quad (6)$$

Obtained by taking logarithms on both sides of the equation (6):

$$\ln(1-\frac{\sigma}{A})=\mathrm{m}\ln\left(\frac{T\text{-}T_\mathrm{r}}{T_\mathrm{m}\text{-}T_\mathrm{r}}\right) \quad (7)$$

Make a curve $\ln(1-\frac{\sigma}{A})$ —$\ln\left(\frac{T-T_\mathrm{r}}{T_\mathrm{m}\text{-}T_\mathrm{r}}\right)$. m is the slope of the curve.

The JC intrinsic parameters of the P110 casing material are shown in Table 1:

Table 1 Parameters of JC ontological model for P110 casing material

A(MPa)	B(MPa)	n	C	m
1163	753.4	0.4509	0.0648	1.53

2.2. Failure modelling of P110 casing materials

The Johnson-Cook failure model combines three factors, namely stress, strain rate, and temperature, and is particularly common in the simulation of ductile metals. The Johnson-Cook damage model defines the failure state of a unit by analyzing the relationship between strain and strain energy at numerous unit integration points on the workpiece, which in turn simulates the real separation process of the abrasive debris [12-14]. The expression of the model can be expressed as:

$$\omega = \int \frac{d\bar{\varepsilon}_p}{\bar{\varepsilon}_p^f} \tag{8}$$

where ω represents the damage parameter; $d\bar{\varepsilon}_p$ represents the integral micrometric increment of the equivalent plastic strain of the grid cell; and $\bar{\varepsilon}_p^f$ represents the equivalent plastic failure strain under critical conditions.

The original expression of the JC damage model can be expressed as:

$$\varepsilon_p^f = \left[d_1 + d_2 \exp\left(d_3 \frac{\sigma_p}{\sigma_m} \right) \right] \times \left[1 + d_4 \ln\left(\frac{\dot{\varepsilon}_p}{\dot{\varepsilon}_o} \right) \right] \times \left[1 + d_5 \left(\frac{T - T_r}{T_{melt} - T_r} \right) \right] \tag{9}$$

Where ε_p^f represents the critical equivalent plastic failure strain, σ_p is the compressive stress (Pa), σ_m is the Mises stress (Pa), $\dot{\varepsilon}_p$ is the strain rate (1/s), and $\dot{\varepsilon}_0$ is the reference strain rate (1/s). d1~d3 denote the material influencing factors of the unit in the x, y, and z directions, d4 denotes the sensitivity parameter of the strain rate, and d5 denotes the influence parameter of the temperature. Parameters d1~d5 are obtained by performing different stress triaxiality experiments at reference strain rate and reference temperature. The JC damage model parameters of P110 casing are shown in Table 2:

Table 2 Parameters of JC damage model for P110 casing material

d1	d2	d3	d4	d5
0.317	5.504	4.161	0.0218	2.326

2.3. Conditional hypothesis

(1) The strength and hardness of the alloy tooth material are much larger than that of the casing material, so it is assumed that the alloy tooth is a rigid body, and the damage to the alloy tooth in the grinding process is not considered.

(2) The alloy teeth and casing are isotropic and uniformly continuous, ignoring the influence of the pore medium, without considering the influence of the environment on the nature of the casing.

(3) Consider only the alloy tooth feed process, and the cutting process of wear chip discharge function is good, the casing failure unit is deleted from the casing body, so do not take into account the impact of the failure of the unit on the subsequent grinding process.

2.4. Finite element modelling

For grinding shoes, the alloy teeth on their surfaces are arranged differently from one shoe to another due to their different shapes, arrangement angles , and surfacing methods. Each alloy tooth can be regarded as a cutter tooth of a milling cutter, and the grinding process of a single alloy tooth is very similar to the metal cutting process, so it can be said that the process of grinding casing with a single alloy tooth is a kind of micro-cutting process. Through the study of the metal-cutting process, the force phenomenon on the surface of the carbide teeth can be understood, which lays the foundation for finding grinding and milling methods to improve grinding efficiency and reduce costs. In summary, because the size, number , and distribution of the alloy teeth of the grinding shoe are very complex, and the grinding and milling process of the grinding shoe can be simplified to the metal cutting process of a single alloy tooth in a short period of time, the complex model of the grinding shoe can be simplified, and the mechanism can be analyzed on the basis of the grinding situation of a single alloy tooth. Through an in-depth study of alloy teeth in the casing grinding movement in the influence of the grinding force and change law, so as to fundamentally understand the role and performance of alloy teeth in the grinding and milling process.

Figure 1 shows the simulation model of the alloy tooth-cutting casing. As shown in the figure, due to a large number of simulation groups, the model is simplified to a two-dimensional plane-cutting model in order to save computational resources and reduce the solution time. The alloy teeth are made of tungsten carbide, and the casing steel grade is P110, and the hardness of the alloy teeth is much larger than that of the casing material, so in order to improve the computational efficiency, the alloy teeth are coupled as a rigid body. Due to the short time length of the analysis step, the circumferential motion of the alloy teeth is simplified to linear motion. The height of the alloy tooth is 0.2×0.3mm, and there exists a front angle θ with the vertical direction of the casing, and the alloy tooth moves from right to left. The casing length is 1×0.5mm, and the bottom of the casing is fully constrained. The model as a whole adopts a four-node bilinear plane stress quadrilateral cell (CPS4R), and in order to improve the computational accuracy, the casing workpiece adopts the local grid encryption technology, i.e., the part of the casing workpiece to be ground is divided by the size of 0.001mm, and the size of the other parts is divided by the size of 0.01mm and the size of the grid division of the alloy teeth is divided by the size of 0.005mm, and the model contains a total of 96736 grids, and the total number of the nodes is The model contains 96736 meshes and the total number of nodes is 97920.

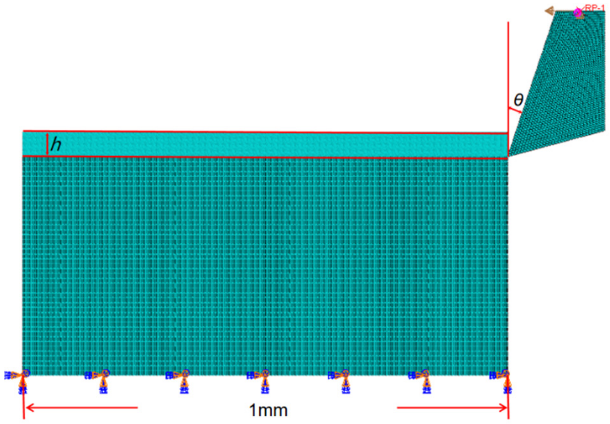

Fig. 1. 2D model of alloy teeth and casing

The alloy teeth and casing material property parameters are shown in Table 3.

Table 3 Alloy teeth and casing material parameters

	Densities (kg/m3)	Poisson's ratio	Young's modulus (GPa)
Alloy teeth	17700	0.3	324
Bushing	7800	0.28	210

3. Finite element results analysis and discussion

3.1. Effect of alloy tooth anterior angle θ on grinding force

Among the alloy tooth geometries, the variation of alloy tooth front angle has the most significant effect on the grinding force [15]. Therefore, we take alloy teeth with different front angles as the object of analysis to explore this effect in depth through 2D orthogonal grinding simulation. Specifically, we will carry out simulations for these alloy teeth in order to understand the force they are subjected to during the grinding process, and how this change affects the final grinding effect. Figure 2 shows the stress distribution and chip shape of the casing workpiece for different alloy teeth' front angles.

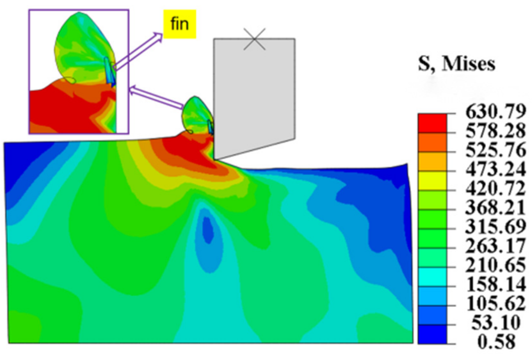

Front angle0°

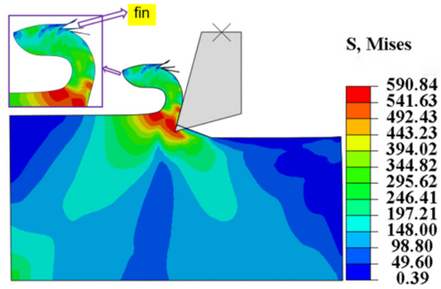

Front angle15°

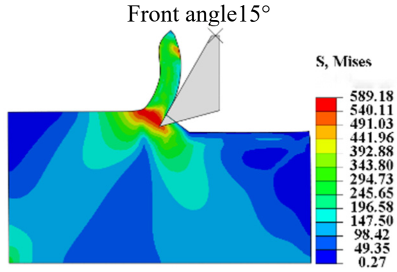

Front angle30°

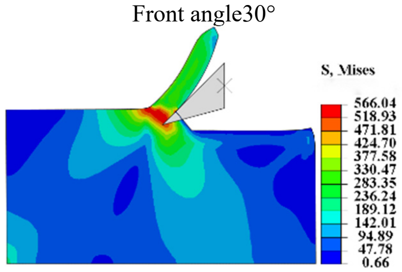

Front angle45°

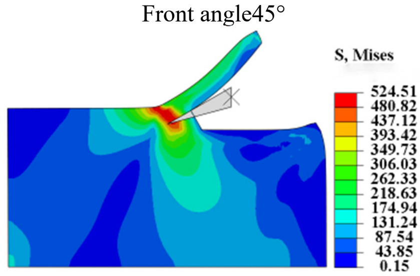

Front angle60°

Fig. 2. Abrasive chip morphology and stress cloud at different alloy tooth front angles

In order to facilitate the calculation, the analysis time of the simulation is set to 0.05s, and all shown in Fig. 2 are the stress distribution states with a motion analysis step of 0.025s. As shown in the figure, the tip of the alloy tooth is first embedded in the casing and produces a local stress concentration phenomenon, and with the time-lapse of the analysis step, the stress spreads inside the casing and the abrasive chips begin to curl. In addition, with the increase of the front angle of the alloy teeth, the friction and extrusion effect of the front surface of the alloy teeth on the casing is reduced, and the abrasive chips are easier to be formed, the maximum Mises stress decreases gradually with the increase of the front angle, and at the same time, the spread of the maximum stress area also decreases, and in the case of the front angle of 0 ° and 15 °, the abrasive chips form a lot of burrs on the surface.

The deformation of abrasive chips can be classified into two types: one is the basic deformation produced by abrasive grinding at the grits, and the other is the tumbling deformation produced by melting and flowing at high temperatures of the workpiece [16]. These two deformations work together to form abrasive chips.

https://doi.org/10.1051/e3sconf/202457301009

During the grinding process, the abrasive swarf often undergoes tumbling and usually breaks automatically after a certain length. This is due to the fact that when the abrasive chips are subjected to deformation, the degree of deformation exceeds the fracture strain limit of the workpiece material, resulting in abrasive chip fracture [17]. Normally, curling deformation alone is not sufficient to reach the fracture strain limit of the material. In the actual grinding process, due to the small distance between the abrasive chip and the grinding part, the abrasive chip will actually break soon due to external force. Therefore, the curling phenomenon of the abrasive chips is less obvious in practical grinding [18].

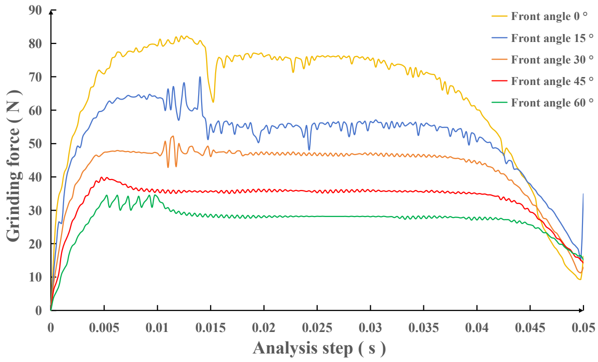

Fig. 3. Grinding forces at different alloy tooth front angles

Figure 3 shows the fluctuation of grinding force during the grinding process for alloy teeth with different rake angles. From the figure, it can be seen that the grinding force decreases significantly with the increase of the leading angle. Grinding time before 0.005s, the grinding force increases sharply, at this time the alloy teeth front angle is embedded inside the casing; in the grinding time of 0.005s, by the cutting vibration, the grinding force begins to enter a stable fluctuation stage, at this time, the highest grinding efficiency; in the grinding time of 0.04s, the grinding force began to decline until the completion of the cutting.

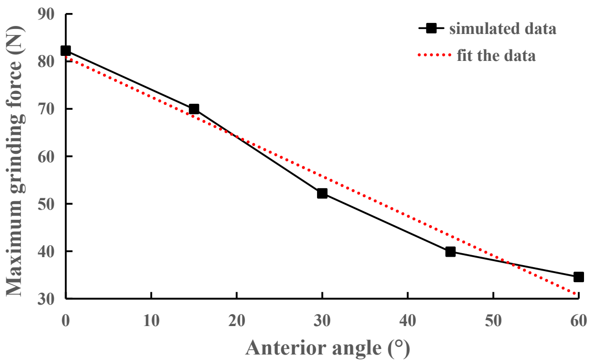

Fig. 4. Fitted curve of grinding force for different alloy tooth front angles

The maximum grinding force during the grinding process of alloy teeth with different front angles was extracted in the simulation post-processing and fitted to the data. Figure 4 represents more intuitively the relationship between the grinding force and the alloy tooth front angle, that is, the grinding force decreases with the increase of the alloy tooth front angle, and the sharper the tip of the alloy tooth is during the grinding process, the smaller the alloy tooth is subjected to the grinding force. The fitted curve is considered a linear function to fit the expression of the relationship between the front angle of the alloy tooth and the grinding force:

$$y = -0.8359x + 80.854 \tag{10}$$

Where x represents the alloy teeth front angle and y represents the grinding force. By fitting out the empirical formula, the force of alloy teeth with different front angles in the downhole can be predicted in advance, which in turn provides theoretical support for the prediction of the torque generated in the grinding and milling process, as well as providing a basis for the selection of the arrangement angle of the alloy teeth on the grinding shoe.

3.2. Influence of grinding depth h on grinding force

With the alloy tooth front angle of 30° unchanged, the grinding depth h was varied so as to investigate the molding state of the abrasive chips and the stress distribution of the casing at different depths. Figure 5 shows the shape of the grinding chips and the stress state of the casing at different depths, and the motion analysis step time is 0.025s.

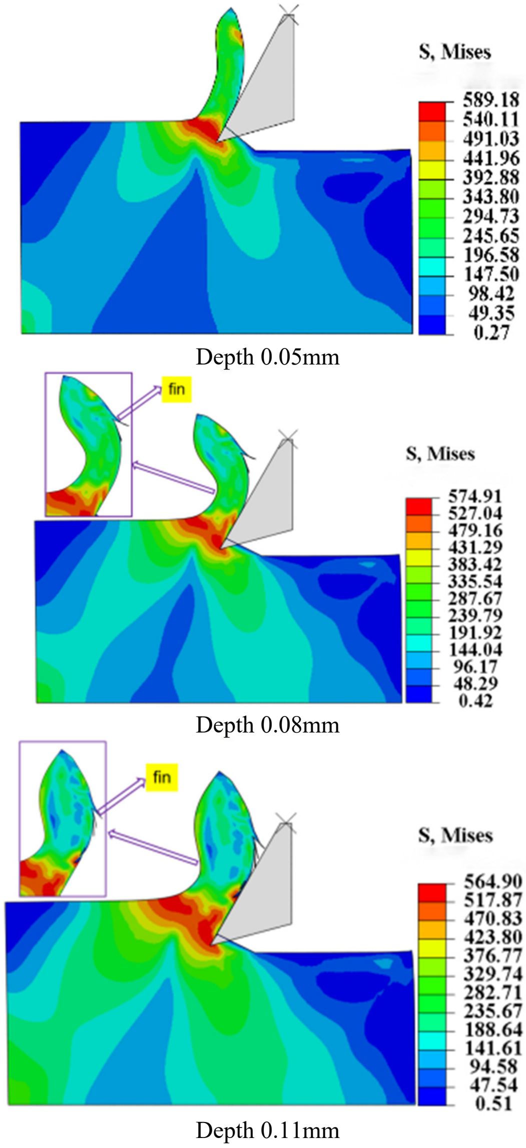

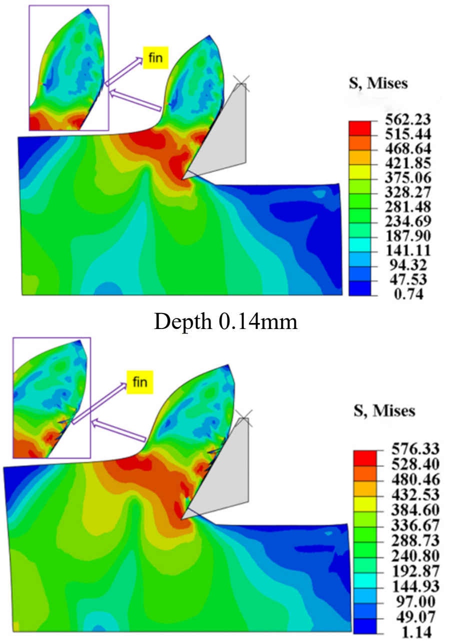

Depth 0.14mm

Depth 0.17mm

Fig. 5. Abrasive chip morphology and stress cloud at different grinding depths

As shown in Fig. 5, the strain on the abrasive chips increases as the depth increases, at which time the abrasive chips are more likely to detach from the surface of the casing and fracture, and burrs are generated on the abrasive chip surface at depths of ~0.08 mm to ~0.17 mm; moreover, the degree of diffusion of the casing's maximum stress region increases significantly with the increase in the depth of the grinding.

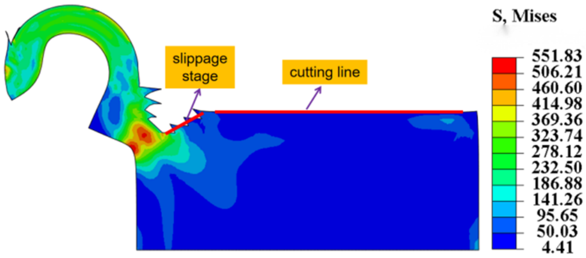

Fig. 6. Abrasive chip morphology and stress cloud at a grinding depth of 0.08 mm

Figure 6 shows the stress and deformation cloud diagram when the grinding depth is 0.08mm, at this time, the motion analysis step has reached 0.05s, and it can be seen that the grinding chip has been generated along the division line slip, indicating that the shear force suffered by the grinding chip at this time is too large, which leads to fracture. In addition, by comparing the casing stress state when the grinding depth is 0.08mm in Fig. 5 and Fig. 6, it can be found that the stress concentration phenomenon is reduced in the latter part of the grinding process, and the grinding force is also reduced at this time, and with the increase of the grinding depth, this phenomenon is more obvious.

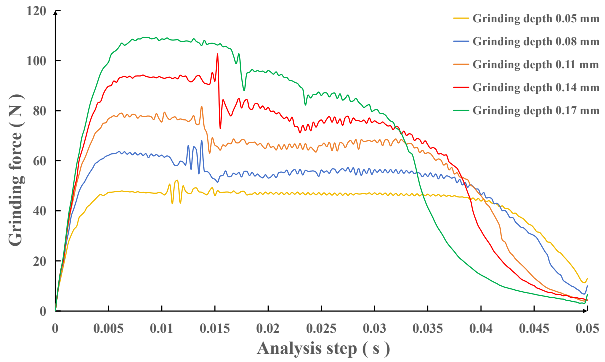

Fig. 7. Grinding forces at different grinding depths

The variation of grinding force at different grinding depths is shown in Fig. 7. It can be seen from the figure that the grinding force increases significantly with the increase of grinding depth. Grinding time before 0.005s, the grinding force increases sharply, at this time the alloy tooth anterior angle is embedded inside the casing; in the grinding time of 0.005s, by the impact of cutting vibration, the grinding force begins to enter a stable fluctuation stage, at this time, the highest efficiency of grinding; in the grinding time of 0.035s, at this time, enter the second half of the grinding process, the grinding force began to decline, the stress concentration phenomenon gradually disappeared, until the completion of the cutting. Until the completion of cutting.

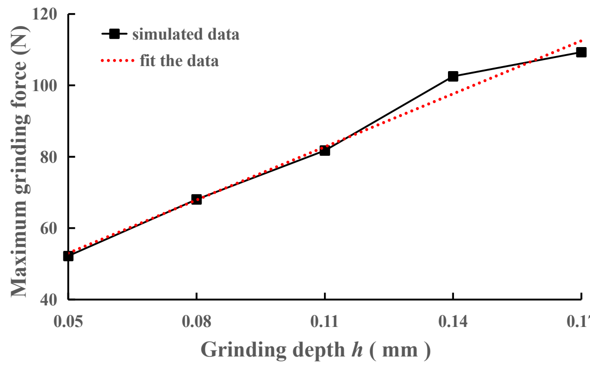

Fig. 8. Fitted curves of grinding force at different grinding depths

The maximum grinding forces during the grinding of alloy teeth at different grinding depths were extracted in the simulation post-processing and fitted to the data. Figure 8 represents more intuitively the relationship between grinding force and grinding depth, i.e., the grinding force increases with the increase of grinding depth. An expression for the relationship between the anterior angle of the alloy tooth and the grinding force was fitted by considering the fitted curve as a linear function:

$$y = 495.47x + 28.259 \tag{11}$$

where x represents the grinding depth and y represents the grinding force. By fitting out the empirical formula, the force on the alloy teeth downhole when embedded in the casing of different depths can be predicted in advance, which in turn provides theoretical support for the prediction of the torque generated during the grinding and milling process, and also provides a basis for the selection of a reasonable grinding depth.

3.3. Effect of grinding speed v on grinding force

Under the actual working condition, the rotational speed is 40 ~ 80r/min, the maximum outer diameter of the grinding shoe is about 106mm, and the linear velocity of the outermost alloy tooth of the grinding shoe is converted to the linear velocity of the alloy tooth, and the rotational speed of the grinding shoe, i.e., the grinding speed of a single alloy tooth, is changed to get the stress on the alloy tooth under the conditions of different rotational speeds with fixed alloy tooth anterior angle of 30° and grinding depth of 0.05mm unchanged. Figure 9 shows the grinding chip morphology and casing stress distribution under different speed conditions, and the motion analysis steps are all 0.0024s, i.e., to ensure that the alloy tooth travels exactly 1mm at the maximum grinding speed.

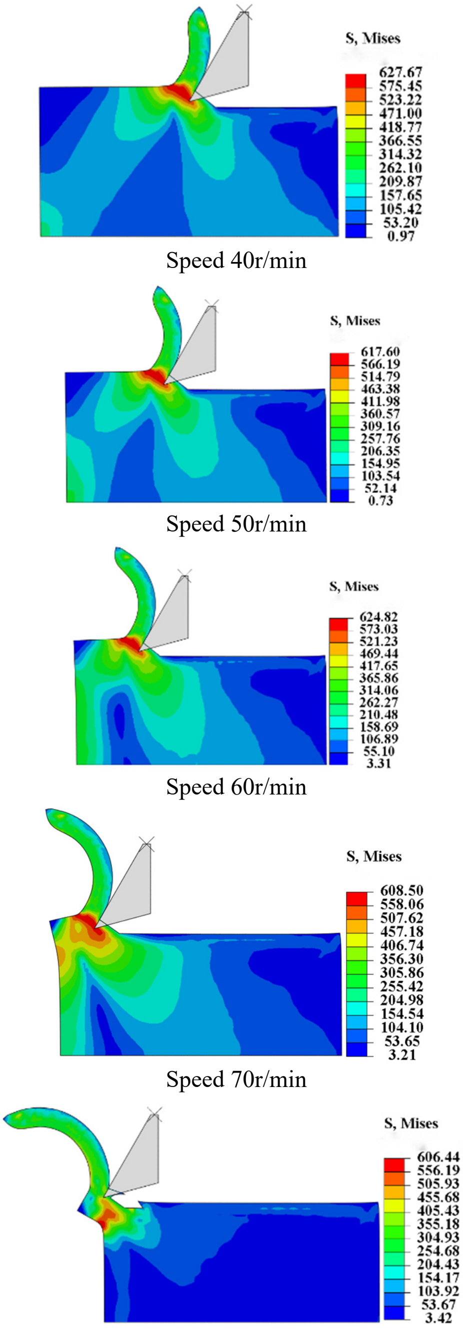

Fig. 9. Wear chip morphology and stress cloud at different rotational speeds at the same time

By comparing the grinding chip morphology and the stress distribution of the casing at different rotational speeds at the same moment, it can be found that: as the rotational speed of the milling shoe increases from 40 to 80 r/min, the stress concentration phenomenon of the casing workpieces is smaller and does not change significantly, in addition, the comparison of the grinding chip morphology is found to be basically the same. Therefore, in the process of low-speed grinding and milling (i.e., the rotational speed is in the range of 40 ~ 80r/min), the influence of rotational speed on the grinding force is small.

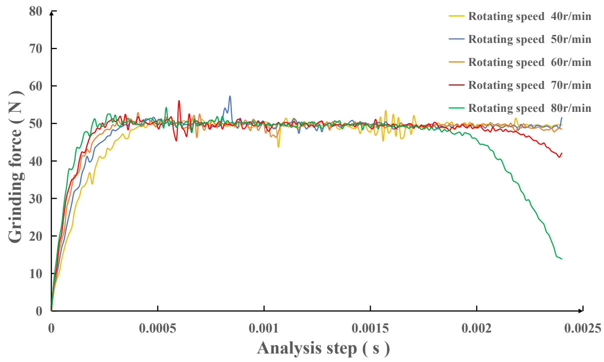

Fig. 10. Grinding force at different speeds

The variation of grinding force at different rotational speeds is shown in Fig. 10. From the figure, it can be seen that the change of grinding force is not obvious in the range of rotational speed 40~ 80r/min. When the grinding time is before 0.0005s, the grinding force increases sharply, and at this time, the anterior angle of the alloy tooth is embedded inside the casing; when the grinding time is 0.0005s, the grinding force starts to enter a stable fluctuation stage under the influence of cutting vibration, and at this time, the grinding efficiency is the highest; when the grinding time is 0.002s, the alloy teeth with the rotational speeds of 70r/min and 80r/min enter into the grinding process. In the second half of the grinding process, the grinding force began to decline, and the stress concentration phenomenon gradually disappeared until the completion of cutting.

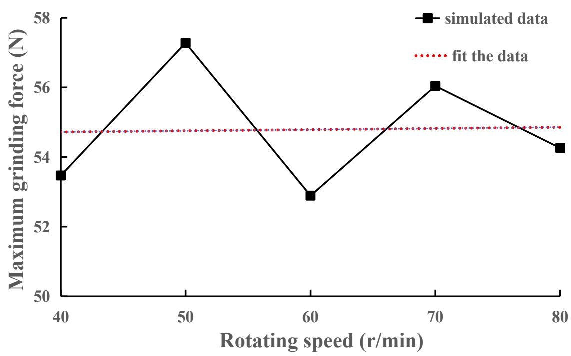

Fig. 11. Fitted curves of grinding force at different rotational speeds

The maximum grinding forces during alloy tooth grinding at different rotational speeds were extracted in the simulation post-processing and fitted to the data. The relationship between grinding force and rotational speed is visualized in Fig. 11, from which it can be seen that the trend of the grinding force is not obvious in the low rotational speed range of 40 r/min ~ and 80 r/min. The

https://doi.org/10.1051/e3sconf/202457301009

expression for the relationship between low rotational speed and grinding force was fitted by considering the fitted curve as a linear function:

$$y = 0.0034x + 54.584 \tag{12}$$

where x represents the rotational speed and y represents the grinding force. By fitting out the empirical formula, the force on the alloy teeth in the well under different rotational speeds can be predicted in advance, which in turn provides theoretical support for the prediction of the torque generated during the grinding and milling process, and also provides a basis for the selection of a reasonable grinding and milling rotational speed.

4. Conclusion

In order to analyze the impact of alloy tooth grinding process parameters on the deformation casing grinding force and its changing law, around the front angle, depth , and speed to carry out sensitivity analysis, research on its factor variables on the alloy tooth in different conditions of the movement and the changing law of grinding force.

(1) As the angle of the front angle of the alloy tooth increases, the friction and extrusion effect of the front surface of the tooth on the casing decreases, which facilitates the shaping of the grinding chip, and at the same time, the degree of diffusion of the maximum stress area decreases, that is to say, the grinding force decreases as the front angle of the alloy tooth increases, and the more pointed the tip of the alloy tooth is during the grinding process, the smaller the alloy tooth suffers from the grinding force.

(2) With the increase of grinding depth, the grinding force increases, and the grinding chips are easy to detach from the casing surface and fracture. At the same time, with the increase of grinding depth, the casing cutting surface plastic deformation effect increases, and the equivalent effect force is concentrated, affected by the shear load, in the second half of the grinding process, the abrasive chips along the division line to produce slip, fracture phenomenon.

(3) In the speed range of 40r/min to 80r/min, the influence of grinding and milling speed on the grinding force is weak, so the efficiency of grinding and milling can be improved by increasing the speed and reducing the grinding time of a single lap in the low-speed range.

References

1. Z. Difei. Ecological Restoration and Transformation of Maoming Oil Shale Mining Area: Experience and Inspirations. Land, 2023, Vol. 12(318): 318.
2. S. Volkan. Conceptual mine design and economic evaluation of mining-assisted heavy oil production of Bati Raman heavy oil field. Arabian Journal of Geosciences, 2023, Vol. 16(9).
3. Y. Hanzhi. Mechanical performance of oil-well cement slurries cured and tested under high-temperatures and high-pressures for deep-well applications. Cement and Concrete Research, 2024, Vol. 175: 107355.
4. T. Zubing. Mechanical Analysis of a Multi-Test String in High-Temperature and High-Pressure Deep Wells. Fluid Dynamics & Materials Processing, 2023, Vol. 19(8): 2161-2170.
5. S. Huan-Yu. Strength analysis of cemented carbide teeth based on ABAQUS. Mechanical and electrical engineering technology, 2020, Vol. 49(4): 44-47.
6. F. Jiaxing. Research and application of mechanical-hydraulic composite casing shaping process technology. Drilling Engineering, 2021, Vol. 48(8): 78-82.
7. W. Zebing. Design and simulation of bionic grinding shoe drilling and grinding composite bridge plug for horizontal well. Petroleum Machinery, 2022, Vol. 50(2): 8-14.
8. D. Kuanhai, L. Wanying. Repairing force for deformed casing shaping with spinning casing swage and damage behaviour of cement sheath. Applied Mathematical Modelling, 2019, Vol. 70: 425-438.
9. M. Aby. The Johnson Cook model for the machinability study. Materials Today: Proceedings, 2023, Vol. 80(1): 357-362.
10. Z. Xiaohua, Z. Bowen. Johnson-Cook ontological model based on orthogonal cutting inverse identification of downhole tubular column. Journal of Central South University (Natural Science Edition), 2024, (3).
11. C. Yinping, K. Zhaofei. Simulation of shear gate performance based on Johnson-Cook model. Petroleum Machinery, 2023, Vol. 51(7): 68-74.
12. W. Chenyu. A modified Johnson-Cook model for 2A12 aluminum alloys. MECHANICS OF TIME-DEPENDENT MATERIALS, 2023.
13. H. Y. Dong. Johnson-Cook (JC) constitutive equation for ZGMn18 high manganese steel. Metalurgija, 2024, Vol. 63(1): 89-92.
14. T. Wenting. The Johnson-Cook Constitutive Model of TA19 Titanium Alloy. Journal of Physics: Conference Series, 2023, Vol. 2557: 012041.
15. J. Chenxi. Analysis of grinding mechanism and influence of working parameters of single-grain milling tools . China University of Petroleum (East China), 2020.
16. W. Jianfei, X. Weihai. Influence of abrasive chips on the micromotional wear behaviour of TC4 titanium alloy. Journal of Tribology, 2022, Vol. 42(5): 1012-1023.
17. W. Long, W. Liuying. Construction and analysis of grinding temperature model for gear grinding by forming method. Journal of Mechanical Engineering, 2022, Vol. 58(3): 295-304.
18. C. Bing, L. Liang. Grinding texture generation mechanism based on grinding trace simulation. China Mechanical Engineering, 2021, Vol. 32(14): 1677-1685.